The Astrophysical Journal, 712:405–420, 2010 March 20 doi:10.1088/0004-637X/712/1/405

MULTIWAVELENGTH OBSERVATIONS OF 3C 454.3. III. EIGHTEEN MONTHS OF *AGILE* MONITORING OF THE "*CRAZY DIAMOND*"

S. Vercellone[1], F. D'Ammando[2,3], V. Vittorini[2,4], I. Donnarumma[2], G. Pucella[5], M. Tavani[2,3,4], A. Ferrari[4,6], C. M. Raiteri[7], M. Villata[7], P. Romano[1], H. Krimm[8,9], A. Tiengo[10], A. W. Chen[4,10], G. Giovannini[11,12], T. Venturi[12], M. Giroletti[12], Y. Y. Kovalev[13,14], K. Sokolovsky[13,14], A. B. Pushkarev[13,15,16], M. L. Lister[17], A. Argan[2], G. Barbiellini[18], A. Bulgarelli[19], P. Caraveo[10], P. W. Cattaneo[20], V. Cocco[2], E. Costa[2], E. Del Monte[2], G. De Paris[2], G. Di Cocco[19], Y. Evangelista[2], M. Feroci[2], M. Fiorini[10], F. Fornari[10], T. Froysland[2], F. Fuschino[19], M. Galli[21], F. Gianotti[19], C. Labanti[19], I. Lapshov[2,22], F. Lazzarotto[2], P. Lipari[23], F. Longo[18], A. Giuliani[10], M. Marisaldi[19], S. Mereghetti[10], A. Morselli[24], A. Pellizzoni[25], L. Pacciani[2], F. Perotti[10], G. Piano[2], P. Picozza[24], M. Pilia[10,25,26], M. Prest[26], M. Rapisarda[5], A. Rappoldi[20], S. Sabatini[2], P. Soffitta[2], E. Striani[2], M. Trifoglio[19], A. Trois[2], E. Vallazza[14], A. Zambra[10], D. Zanello[23], C. Pittori[27], F. Verrecchia[27], P. Santolamazza[27], P. Giommi[27], S. Colafrancesco[27], L. Salotti[28], I. Agudo[29], H. D. Aller[30], M. F. Aller[30], A. A. Arkharov[15], U. Bach[13], R. Bachev[31], P. Beltrame[32], E. Benítez[33], M. Böttcher[34], C. S. Buemi[35], P. Calcidese[36], D. Capezzali[37], D. Carosati[37], W. P. Chen[38], D. Da Rio[32], A. Di Paola[39], M. Dolci[40], D. Dultzin[33], E. Forné[41], J. L. Gómez[29], M. A. Gurwell[42], V. A. Hagen-Thorn[43,44], A. Halkola[45], J. Heidt[46], D. Hiriart[33], T. Hovatta[47], H.-Y. Hsiao[38], S. G. Jorstad[48], G. Kimeridze[49], T. S. Konstantinova[43], E. N. Kopatskaya[43], E. Koptelova[38], O. Kurtanidze[49], A. Lähteenmäki[47], V. M. Larionov[15,43,44], P. Leto[35], R. Ligustri[32], E. Lindfors[45], J. M. Lopez[33], A. P. Marscher[48], R. Mujica[50], M. Nikolashvili[49], K. Nilsson[45], M. Mommert[46], N. Palma[34], M. Pasanen[45], M. Roca-Sogorb[29], J. A. Ros[41], P. Roustazadeh[34], A. C. Sadun[51], J. Saino[45], L. Sigua[49], M. Sorcia[33], L. O. Takalo[45], M. Tornikoski[47], C. Trigilio[35], R. Turchetti[32], and G. Umana[35]

[1] INAF/IASF–Palermo, Via U. La Malfa 153, I-90146 Palermo, Italy; stefano@ifc.inaf.it
[2] INAF/IASF–Roma, Via del Fosso del Cavaliere 100, I-00133 Roma, Italy
[3] Dip. di Fisica, Univ. "Tor Vergata," Via della Ricerca Scientifica 1, I-00133 Roma, Italy
[4] CIFS–Torino, Viale Settimio Severo 3, I-10133 Torino, Italy
[5] ENEA–Roma, Via E. Fermi 45, I-00044 Frascati (Roma), Italy
[6] Dip. di Fisica, Univ. di Torino, Via P. Giuria 1, I-10125 Torino, Italy
[7] INAF, Osservatorio Astronomico di Torino, Via Osservatorio 20, I-10025 Pino Torinese, Italy
[8] CRESST and NASA Goddard Space Flight Center, Greenbelt, MD, USA
[9] Universities Space Research Association, Columbia, MD, USA
[10] INAF/IASF–Milano, Via E. Bassini 15, I-20133 Milano, Italy
[11] Dip. di Astronomia, Univ. di Bologna, via Ranzani 1, I-40127 Bologna, Italy
[12] INAF/IRA, via Gobetti 101, I-40129 Bologna, Italy
[13] Max-Planck-Institut für Radioastronomie, Auf dem Hügel 69, 53121 Bonn, Germany
[14] Astro Space Center of Lebedev Physical Institute, Profsoyuznaya 84/32, 117997 Moscow, Russia
[15] Pulkovo Observatory, St. Petersburg, Russia
[16] Crimean Astrophysical Observatory, 98049 Nauchny, Crimea, Ukraine
[17] Purdue University, 520 NW Avenue, West Lafayette, IN 47906, USA
[18] Dip. di Fisica and INFN, Via Valerio 2, I-34127 Trieste, Italy
[19] INAF/IASF–Bologna, Via Gobetti 101, I-40129 Bologna, Italy
[20] INFN–Pavia, Via Bassi 6, I-27100 Pavia, Italy
[21] ENEA–Bologna, Via Martiri di Monte Sole 4, I-40129 Bologna, Italy
[22] IKI, Academy of Sciences, Moscow, Russia
[23] INFN–Roma "La Sapienza", Piazzale A. Moro 2, I-00185 Roma, Italy
[24] INFN–Roma "Tor Vergata", Via della Ricerca Scientifica 1, I-00133 Roma, Italy
[25] INAF, Osservatorio Astronomico di Cagliari, località Poggio dei Pini, strada 54, I-09012 Capoterra, Italy
[26] Dipartimento di Fisica, Università dell'Insubria, Via Valleggio 11, I-22100 Como, Italy
[27] ASI–ASDC, Via G. Galilei, I-00044 Frascati (Roma), Italy
[28] ASI, Viale Liegi 26, I-00198 Roma, Italy
[29] Instituto de Astrofísica de Andalucía, CSIC, Spain
[30] Department of Astronomy, University of Michigan, MI, USA
[31] Institute of Astronomy, Bulgarian Academy of Sciences, Bulgaria
[32] Circolo Astrofili Talmassons, Italy
[33] Instituto de Astronomía, Universidad Nacional Autónoma de México, Mexico
[34] Astrophysical Institute, Department of Physics and Astronomy, Ohio University, Athens, OH, USA
[35] INAF, Osservatorio Astrofisico di Catania, Italy
[36] Osservatorio Astronomico della Regione Autonoma Valle d'Aosta, Italy
[37] Armenzano Astronomical Observatory, Italy
[38] Institute of Astronomy, National Central University, Taiwan
[39] INAF, Osservatorio Astronomico di Roma, Italy
[40] INAF, Osservatorio Astronomico di Collurania Teramo, Italy
[41] Agrupació Astronòmica de Sabadell, Spain
[42] Harvard-Smithsonian Center for Astrophysics, MA, USA
[43] Astronomical Institute, St. Petersburg State University, Russia
[44] Isaac Newton Institute of Chile, St. Petersburg Branch, Russia
[45] Tuorla Observatory, Department of Physics and Astronomy, University of Turku, Finland
[46] ZAH, Landessternwarte Heidelberg-Königstuhl, Germany
[47] Metsähovi Radio Observatory, Helsinki University of Technology TKK, Finland

[48] Institute for Astrophysical Research, Boston University, MA, USA
[49] Abastumani Astrophysical Observatory, Georgia
[50] INAOE, Mexico
[51] Department of Physics, University of Colorado, Denver, CO, USA
Received 2009 October 14; accepted 2010 February 4; published 2010 March 2

ABSTRACT

We report on 18 months of multiwavelength observations of the blazar 3C 454.3 (*Crazy Diamond*) carried out in the period 2007 July–2009 January. In particular, we show the results of the *AGILE* campaigns which took place on 2008 May–June, 2008 July–August, and 2008 October–2009 January. During the 2008 May–2009 January period, the source average flux was highly variable, with a clear fading trend toward the end of the period, from an average γ-ray flux $F_{\rm E>100\,MeV} \gtrsim 200 \times 10^{-8}$ photons cm^{-2} s^{-1} in 2008 May–June, to $F_{\rm E>100\,MeV} \sim 80 \times 10^{-8}$ photons cm^{-2} s^{-1} in 2008 October–2009 January. The average γ-ray spectrum between 100 MeV and 1 GeV can be fit by a simple power law, showing a moderate softening (from $\Gamma_{\rm GRID} \sim 2.0$ to $\Gamma_{\rm GRID} \sim 2.2$) toward the end of the observing campaign. Only 3σ upper limits can be derived in the 20–60 keV energy band with Super-*AGILE*, because the source was considerably off-axis during the whole time period. In 2007 July–August and 2008 May–June, 3C 454.3 was monitored by *Rossi X-ray Timing Explorer* (*RXTE*). The *RXTE*/Proportional Counter Array (PCA) light curve in the 3–20 keV energy band shows variability correlated with the γ-ray one. The *RXTE*/PCA average flux during the two time periods is $F_{3-20\,\rm keV} = 8.4 \times 10^{-11}$ erg cm^{-2} s^{-1}, and $F_{3-20\,\rm keV} = 4.5 \times 10^{-11}$ erg cm^{-2} s^{-1}, respectively, while the spectrum (a power law with photon index $\Gamma_{\rm PCA} = 1.65 \pm 0.02$) does not show any significant variability. Consistent results are obtained with the analysis of the *RXTE*/High-Energy X-Ray Timing Experiment quasi-simultaneous data. We also carried out simultaneous *Swift* observations during all *AGILE* campaigns. *Swift*/XRT detected 3C 454.3 with an observed flux in the 2–10 keV energy band in the range (0.9–7.5) $\times 10^{-11}$ erg cm^{-2} s^{-1} and a photon index in the range $\Gamma_{\rm XRT} = 1.33$–2.04. In the 15–150 keV energy band, when detected, the source has an average flux of about 5 mCrab. GASP-WEBT monitored 3C 454.3 during the whole 2007–2008 period in the radio, millimeter, near-IR, and optical bands. The observations show an extremely variable behavior at all frequencies, with flux peaks almost simultaneous with those at higher energies. A correlation analysis between the optical and the γ-ray fluxes shows that the γ-optical correlation occurs with a time lag of $\tau = -0.4^{+0.6}_{-0.8}$ days, consistent with previous findings for this source. An analysis of 15 GHz and 43 GHz VLBI core radio flux observations in the period 2007 July–2009 February shows an increasing trend of the core radio flux, anti-correlated with the higher frequency data, allowing us to derive the value of the source magnetic field. Finally, the modeling of the broadband spectral energy distributions for the still unpublished data, and the behavior of the long-term light curves in different energy bands, allow us to compare the jet properties during different emission states, and to study the geometrical properties of the jet on a time-span longer than one year.

Key words: galaxies: active – galaxies: jets – quasars: general – quasars: individual (3C 454.3) – radiation mechanisms: non-thermal

Online-only material: color figures, machine-readable table

1. INTRODUCTION

Among active galactic nuclei (AGNs), blazars show intense and variable γ-ray emission above 100 MeV (Hartman et al. 1999), with variability timescales as short as a few days, or a few weeks.

Blazars emit across several decades of energy, from the radio to the TeV energy band, and their spectral energy distributions (SEDs) typically show two distinct humps. The first peak occurs in the IR/optical band in the Flat Spectrum Radio Quasars (FSRQs) and in the Low-energy peaked BL Lacs (LBLs), and at UV/X-rays in the High-energy peaked BL Lacs (HBLs). The second hump peaks at MeV–GeV and TeV energies in FSRQs/LBLs and in HBLs, respectively. In the framework of leptonic models, the first peak is commonly interpreted as synchrotron radiation from high-energy electrons in a relativistic jet, while the second peak is interpreted as inverse Compton (IC) scattering of soft seed photons by the same relativistic electrons. A recent review of the blazar emission mechanisms and energetics is given in Celotti & Ghisellini (2008). Alternatively, the blazar SED can be explained in the framework of the hadronic models, where the relativistic protons in the jet are the primary accelerated particles, emitting γ-ray radiation by means of photo-pair and photo-pion production (see Mücke & Protheroe 2001; Mücke et al. 2003 for a review on hadronic models).

Since the launch of *AGILE*, the FSRQ 3C 454.3 (PKS 2251+158; $z = 0.859$) became one of the most active sources in the γ-ray sky. Its very high γ-ray flux (well above 100×10^{-8} photons cm^{-2} s^{-1} for $E > 100$ MeV), its flux variability (on a timescale of 1 or 2 days), and the fact that it was always detected during any *AGILE* pointing, made it earn the nickname of *Crazy Diamond*: 3C 454.3 is now playing the same role as 3C 279 had for *EGRET* (e.g., Hartman et al. 2001a, 2001b).

Multiwavelength studies of variable γ-ray blazars are crucial in order to understand the physical processes responsible for the emission along the whole spectrum. Since the detection of the exceptional 2005 outburst (see Giommi et al. 2006; Fuhrmann et al. 2006; Pian et al. 2006), several monitoring campaigns were carried out to follow the source multifrequency behavior (Villata et al. 2006, 2007; Raiteri et al. 2007, 2008a, 2008b). In mid 2007 July, 3C 454.3 underwent a new optical brightening, which triggered observations at all frequencies. *AGILE* performed a target of opportunity (ToO) re-pointing toward the source and detected it in a very high γ-ray state

(Vercellone et al. 2008, hereafter V08). In 2007 November and December, *AGILE* detected high γ-ray activity from 3C 454.3, triggering multiwavelength ToO campaigns, whose results are reported in Vercellone et al. (2009, hereafter Paper I), in Donnarumma et al. (2009, hereafter Paper II), and in Anderhub et al. (2009), respectively. Paper I and Paper II demonstrated that to fit the simultaneous broadband SEDs from radio to γ-ray data, IC scattering of external photons from the broad-line region (BLR) off the relativistic electrons in the jet was required. In an earlier work based on the Vercellone et al. (2007) preliminary flux estimate of the 2007 July flare, Ghisellini et al. (2007) made a comparison between the 3C 454.3 SEDs in 2000 (*EGRET* data), 2005 (optical and X-ray flare), and 2007 (*AGILE* γ-ray flare), discussing the role of the bulk Lorentz factor Γ (associated with the emitting source compactness) during the different epochs.

Moreover, the results of a correlation analysis performed in Paper I was consistent with no time-lags between the γ-ray and the optical flux variations. Such a result was recently confirmed by Bonning et al. (2009) who correlated optical, UV, X-ray, and γ-ray[52] data. In a very recent paper, Abdo et al. (2009) show the results of the first three months of *Fermi* observations of 3C 454.3, from 2008 July to October. They present for the first time the signature of a spectral break above a few GeV, interpreted as a possible break in the energy distribution of the emitting particles.

In this paper (Paper III), we present both a re-analysis of the *AGILE* published data collected during the period 2007 July–2007 December, and the results of multiwavelength campaigns on 3C 454.3 during a long-lasting γ-ray activity period between 2008 May 10 and 2009 January 12. In particular, we show the results of the *AGILE* campaigns which took place on 2008 May–June (mj08), 2008 July–August (ja08), and 2008 October–2009 January (oj09). Preliminary γ-ray results were distributed in Donnarumma et al. (2008); Vittorini et al. (2008); Gasparrini et al. (2008); Pittori et al. (2008), while radio-to-optical data were published in Villata et al. (2009).

This paper is organized as follows. In Sections 2–6 we present the *AGILE*, *Swift*, *Rossi X-ray Timing Explorer* (*RXTE*), *GLAST-AGILE* Support Program within the Whole Earth Blazar Telescope (GASP-WEBT), and radio VLBI data analysis and results. In Section 7, we present the simultaneous multiwavelength light curves. In Sections 8 and 9, we discuss the results and draw our conclusions. Throughout this paper the quoted uncertainties are given at the 1σ level, unless otherwise stated, and we adopted a ΛCDM cosmology with the following values for the cosmological parameters: $h = 0.71$, $\Omega_m = 0.27$, and $\Omega_\Lambda = 0.73$.

2. *AGILE* DATA

2.1. Data Reduction and Analysis

The *AGILE* satellite (Tavani et al. 2008, 2009), a mission of the Italian Space Agency (ASI) devoted to high-energy astrophysics, is currently the only space mission capable of observing cosmic sources simultaneously in the energy bands 18–60 keV and 30 MeV–50 GeV.

The *AGILE* scientific instrument combines four active detectors yielding broadband coverage from hard X-rays to γ-rays: a Silicon Tracker (ST; Prest et al. 2003, 30 MeV–50 GeV), a co-aligned coded-mask hard X-ray imager, Super-*AGILE* (SA; Feroci et al. 2007, 18–60 keV), a non-imaging CsI Mini-Calorimeter (MCAL; Labanti et al. 2009, 0.3–100 MeV), and a segmented Anti-Coincidence System (ACS; Perotti et al. 2006). Gamma-ray detection is obtained by the combination of ST, MCAL, and ACS; these three detectors form the *AGILE* Gamma-Ray Imaging Detector (GRID).

Level-1 *AGILE*-GRID data were analyzed using the *AGILE* Standard Analysis Pipeline (see V08 for a detailed description of the *AGILE* data reduction). Since 3C 454.3 was observed at high off-axis angle due to the satellite solar panel constraints, an ad hoc γ-ray analysis was performed. We used γ-ray events filtered by means of the `FM3.119_2a` *AGILE* Filter pipeline. Counts, exposure, and Galactic background γ-ray maps were created with a bin size of $0.^\circ25 \times 0.^\circ25$, for $E \geqslant 100$ MeV. Since the source was observed up to 40° off-axis, all the maps were generated including all events collected up to 60° off-axis. We rejected all γ-ray events whose reconstructed directions form angles with the satellite-Earth vector smaller than 85°, reducing the γ-ray Earth albedo contamination by excluding regions within $\sim 15^\circ$ from the Earth limb. We used the version (`BUILD-16`) of the Calibration files (`I0006`), which are publicly available at the ASI Science Data Centre (ASDC) Web site,[53] and of the γ-ray diffuse emission model (Giuliani et al. 2004). We ran the *AGILE* Source Location task in order to derive the most accurate location of the source. Then, we ran the *AGILE* Maximum Likelihood Analysis (`ALIKE`) using a radius of analysis of 10°, and the best guess position derived in the first step. The particular choice of the analysis radius is dictated to avoid any possible contamination from very off-axis residual particle events.

Table 1
AGILE/GRID Observation Log

Epoch	Start Time (UTC)	End Time (UTC)	Exposure (Ms)
1	2007 Jul 24 14:30	2007 Jul 30 11:40	0.22
2	2007 Nov 10 12:16	2007 Dec 01 11:38	0.64
3	2007 Dec 01 11:39	2007 Dec 16 12:09	0.56
4	2008 May 10 11:00	2008 Jun 09 15:20	1.03
5, 6	2008 Jun 15 10:46	2008 Jun 30 11:14	0.54
7	2008 Jul 25 19:57	2008 Aug 14 21:08	0.70
8	2008 Oct 17 12:51	2009 Jan 12 14:30	2.86

2.2. GRID Results

Table 1 shows the *AGILE*/GRID observation log during the different time periods. We have re-analyzed all the *AGILE* data already published in V08, Paper I, and Paper II, respectively, according to the procedure described in Section 2.1. The results are discussed in Section 7. In the following paragraphs we report the detailed results of the still unpublished *AGILE* data.

2.2.1. 2008 May–June

The *AGILE* campaign was split into two different periods, May 10–June 9 (P1) and June 15–30 (P2) because of a ToO re-pointing toward W Comae. The total on-source exposure is 1.03 (P1) + 0.54 (P2) Ms. 3C 454.3 was detected, during P1 and P2, at a 25.6σ and 16.3σ level with an average flux of $F^{\rm P1}_{\rm E>100\ MeV} = (218 \pm 12) \times 10^{-8}$ photons cm^{-2} s^{-1}, and $F^{\rm P2}_{\rm E>100\ MeV} = (198 \pm 17) \times 10^{-8}$ photons cm^{-2} s^{-1} , respectively, as derived from the *AGILE* Maximum Likelihood Code analysis.

[52] The γ-ray data are taken from the *Fermi*/LAT monitored source list light curves available at http://fermi.gsfc.nasa.gov/ssc/data/access/.

[53] http://agile.asdc.asi.it

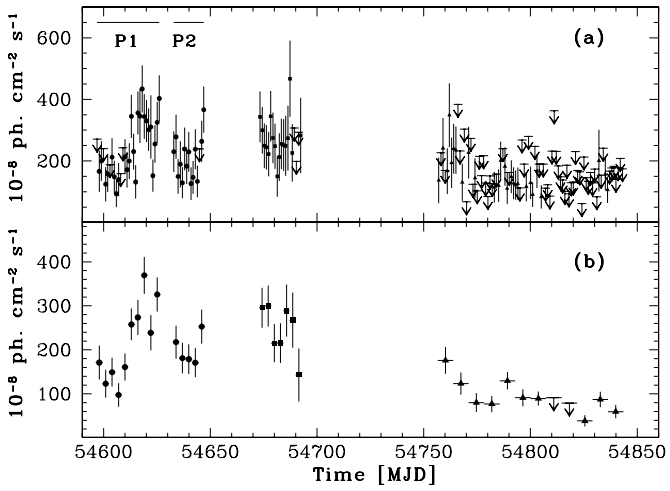

Figure 1. (a): *AGILE*/GRID γ-ray light curve at $\approx$ 1 day resolution for $E > 100$ MeV in units of 10^{-8} photons cm^{-2} s^{-1} during the period 2008 May–2009 January. The downward arrows represent 2σ upper limits. (b): Same as in (a), but with a time bin of 3 (filled circles and squares), and 7 (filled triangles) days, respectively.

Figure 1, filled circles in panel (a), shows the γ-ray light curve at 1 day resolution for photons above 100 MeV. We note that, particularly at the beginning of the campaign, 3C 454.3 was not always detected on a day-by-day timescale. On MJD $\sim$ 54610 the source began to be detected at a 3σ level almost continuously; this clearly indicates the onset of a γ-ray flaring activity.

The average γ-ray flux as well as the daily values were derived according to the γ-ray analysis procedure described in Mattox et al. (1993). First, the entire period was analyzed to determine the diffuse gas parameters and then the source flux density was estimated independently for each of the eighteen 1 day periods with the diffuse parameters fixed at the values previously obtained.

Figure 1, panel (b), shows the same *AGILE*/GRID data binned on a timescale of 3 days. The light curve clearly shows a strong degree of variability, with a dynamic range of about four in about two weeks.

Figure 2, panel (a), shows the average γ-ray spectra extracted over the observing periods P1 and P2. Each average spectrum was obtained by computing the γ-ray flux in five energy bins over each period: 50 MeV $< E <$ 100 MeV, 100 MeV $< E <$ 200 MeV, 200 MeV $< E <$ 400 MeV, 400 MeV $< E <$ 1000 MeV, and 1000 MeV $< E <$ 3000 MeV. We note that the current instrument response is accurately calibrated in the energy band 100 MeV–1 GeV, and that the flux above 1 GeV is underestimated by a factor of about 2. For those reasons, we fit the data by means of a simple power-law model and restricted our fit to the 100 MeV–1 GeV energy range, obtaining

$$F^{\rm P1}(E) = 2.63 \times 10^{-4} \times \left(\frac{E}{1\,{\rm MeV}}\right)^{-(2.05\pm0.10)} \text{photons cm}^{-2}\text{s}^{-1}\,\text{MeV}^{-1}, \quad (1)$$

$$F^{\rm P2}(E) = 1.58 \times 10^{-4} \times \left(\frac{E}{1\,{\rm MeV}}\right)^{-(1.98\pm0.16)} \text{photons cm}^{-2}\text{s}^{-1}\,\text{MeV}^{-1}. \quad (2)$$

The different energy range, and, above all, the different time period, could explain the different value of the *AGILE* (2.05 ± 0.10 and 1.98 ± 0.16) and *Fermi*/LAT (2.27 ± 0.03 , pre-break; Abdo et al. 2009) γ-ray photon indices.

2.2.2. 2008 July–August

The *AGILE* campaign started immediately after the *Fermi*/LAT detection of a very high γ-ray activity in the period 2008 July 10–21 (Tosti et al. 2008), which reached, on July 10, a γ-ray flux of $F^{\rm Fermi}_{\rm E>100\ MeV} = 1200 \times 10^{-8}$ photons cm^{-2} s^{-1} (Abdo et al. 2009). The *AGILE* observations covered the period from 2008 July 25 19:57 UT to 2008 August 14 21:08 UT, for a total on-source exposure of about 0.71 Ms. 3C 454.3 was detected at a 17.5σ level with an average flux of $F^{\rm ja08}_{\rm E>100\ MeV} = (255 \pm 21) \times 10^{-8}$ photons cm^{-2} s^{-1}, as derived from the *AGILE* Maximum Likelihood Code analysis.

Figure 1, filled squares in panel (a) and in panel (b), shows the γ-ray light curve at 1 day and at 3 day resolution, respectively, for photons above 100 MeV. The average γ-ray flux as well as the daily values were derived according to the procedure described in Section 2.2.1. Contrary to the May–June data, the July–August light curve does not show any clear sign of variability.

Figure 2, panel (b), shows the average γ-ray spectrum derived over the entire observing period. The average spectrum was obtained by computing the γ-ray flux in the same way as in Section 2.2.1. We fit the data by means of a simple power-law model and restricted our fit to the most reliable energy range (100 MeV–1 GeV):

$$F^{\rm ja08}(E) = 3.96 \times 10^{-4} \times \left(\frac{E}{1\,{\rm MeV}}\right)^{-(2.11\pm0.14)} \text{photons cm}^{-2}\text{s}^{-1}\,\text{MeV}^{-1}. \quad (3)$$

During this period, which partially overlaps with the *Fermi* one, the *AGILE* γ-ray photon index is, within the statistical errors, in agreement with the *Fermi*/LAT result.

2.2.3. 2008 October–2009 January

The *AGILE* observations covered the period from 2008 October 17 12:51 UT to 2009 January 12 14:30 UT, for a total on-source exposure of about 2.86 Ms. 3C 454.3 was detected at a 17.9σ level with an average flux of $F^{\rm oj09}_{E>100\ \rm MeV} = (77 \pm 5) \times 10^{-8}$ photons cm^{-2} s^{-1}, as derived from the *AGILE* Maximum Likelihood Code analysis.

Figure 1, filled triangles in panel (a), shows the γ-ray light curve at 1 day resolution for photons above 100 MeV. The average γ-ray flux as well as the daily values were derived according to the procedure described in Section 2.2.1. The light curve does not show any clear trend, partly because of a dominant fraction of upper limits in the data. For this reason, we decided to rebin the light curve on a timescale of one week. The resulting light curve is shown in Figure 1, filled triangles in panel (b). On this timescale, a clear trend is present, with the source dimming as a function of time, with a dynamic range of about a factor of 2.

Figure 2, panel (c), shows the average γ-ray spectrum derived over the entire observing period. The average spectrum was obtained by computing the γ-ray flux in the same way as in Section 2.2.1. We fit the data by means of a simple power-law

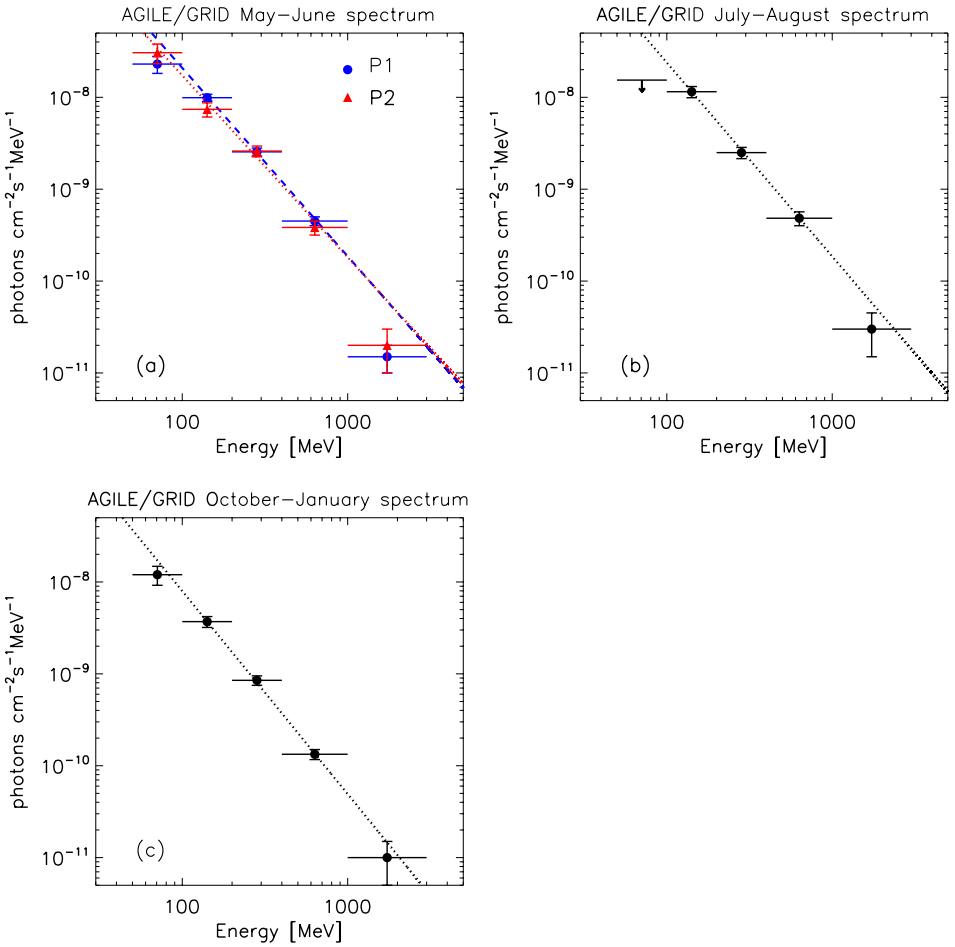

Figure 2. (a): *AGILE*/GRID average γ-ray spectrum for periods P1 and P2. The blue-dashed and the red-dotted lines represent the best-fit power-law models for P1 and P2, respectively. (b) and (c) show the average γ-ray spectra during the periods 2008 July–August and 2008 October–2009 January, respectively. In the three panels only three energy bins were considered for the spectral fitting: $100 < E < 200$ MeV, $200 < E < 400$ MeV, $400 < E < 1000$ MeV (see the text for details).
(A color version of this figure is available in the online journal.)

Table 2
Super-*AGILE* Observation Results

Start Time (UTC)	End Time (UTC)	θ_X (deg)	θ_Z (deg)	Exposure (ks)	$F_{20-60\,keV}$ (mCrab)
2008 May 31 10:18	2008 Jun 09 13:38	−23.0	+06.0	380	<16
2008 Jun 15 14:11	2008 Jun 21 12:59	−36.0	+08.0	270	<18
2008 Jul 25 21:39	2008 Aug 02 23:29	+03.4	−42.0	345	<18
2008 Oct 17 18:47	2008 Oct 29 23:12	−00.8	−45.0	460	<21

model and restricted our fit to the most reliable energy range (100 MeV–1 GeV):

$$F^{\rm oj09}(E) = 2.10 \times 10^{-4} \times \left(\frac{E}{1\,\rm MeV}\right)^{-(2.21\pm0.13)} \text{photons cm}^{-2}\,\text{s}^{-1}\,\text{MeV}^{-1}. \quad (4)$$

2.3. Super-AGILE Results

During the various *AGILE* pointings, 3C 454.3 was located substantially off-axis in the Super-*AGILE* field of view (FoV). For this reason, only 3σ upper limits can be derived in the 20–60 keV energy band during the *AGILE*/GRID observations. Table 2 summarizes the Super-*AGILE* observations and their results.

3. *SWIFT* DATA

3.1. Data Reduction and Analysis

Swift pointed observations (Gehrels et al. 2004) were performed from 2007 July 26 to 2009 January 1. These observations were obtained both by means of several dedicated ToOs (P.I.: S. Vercellone) and by activating *Swift* Cycle-3 (Obs. ID 00031018, P.I.: A.W. Chen) and Cycle-4 Proposals (Obs. ID 00031216, P.I.: S. Vercellone). A long-lasting monitoring program (P.I.s: L. Fuhrmann and S. Vercellone) covers the period 2008 July–October.

3.1.1. Swift/XRT

Table 3 summarizes the *Swift*/XRT observations. The XRT data were processed with standard procedures (`xrtpipeline` ver. 0.12.1), adopting the standard filtering and screening

Table 3
Swift/XRT Observation Log

Sequence	Obs. Mode	Start time (UT) (yyyy mm dd hh:mm:ss)	End time (UT) (yyyy mm dd hh:mm:ss)	Exp.[a] (s)
(1)	(2)	(3)	(4)	(5)
00035030013	PC	2007 Jul 26 00:55:44	2007 Jul 26 01:13:58	1073
00035030014	PC	2007 Jul 28 07:26:46	2007 Jul 28 10:44:55	817
00035030015	PC	2007 Jul 30 10:59:09	2007 Jul 30 14:16:56	897
00035030016	PC	2007 Aug 01 11:05:10	2007 Aug 01 11:07:58	168
00035030017	WT	2007 Aug 01 09:33:17	2007 Aug 01 13:06:59	3903

Note. [a] The exposure time is spread over several snapshots during each observations.

(This table is available in its entirety in a machine-readable form in the online journal. A portion is shown here for guidance regarding its form and content.)

criteria, and using FTOOLS in the `Heasoft` package (ver. 6.6.1). The source count rate was variable during the campaigns, ranging from 0.26 to 1.8 counts s^{-1}. For this reason, we considered both photon counting (PC) and windowed timing (WT) data, and further selected XRT event grades 0–12 and 0–2 for the PC and WT events, respectively (Burrows et al. 2005). Several *Swift*/XRT observations showed an average count rate of > 0.5 counts s^{-1}, therefore in these cases pile-up correction was required for the PC data. We extracted the source events from an annular region with an inner radius of 3 pixels (estimated by means of the point-spread function (PSF) fitting technique) and an outer radius of 30 pixels (1 pixel $\sim$ 2.″36). When the average count rate was < 0.5 counts s^{-1}, we used the full 30 pixel radius region.

We also extracted background events within an annular region centered on the source with radii of 110 and 160 pixels. Ancillary response files were generated with `xrtmkarf`, and account for different extraction regions, vignetting and PSF corrections. We used the spectral redistribution matrices ver. 011 in the Calibration Database maintained by HEASARC. *Swift*/XRT uncertainties are given at 90% confidence level for one interesting parameter (i.e., $\Delta\chi^2 = 2.71$) unless otherwise stated.

The *Swift*/XRT spectra were rebinned in order to have at least 20 counts per energy bin. We fit the spectra with an absorbed power-law model (`wabs*(powerlaw)` in `XSPEC 11.3.2`). The Galactic absorption was fixed to the value of $N_{\rm H}^{\rm Gal} = 1.34 \times 10^{21}$ cm^{-2}, as obtained by Villata et al. (2006) by means of a deep *Chandra* observation. We note the adopted value is consistent with the mean of the distribution of the $N_{\rm H}$ values obtained by fitting the spectra with an absorbed power-law model and free absorption.

3.1.2. *Swift*/*UVOT*

The Ultraviolet/Optical Telescope (UVOT) data analysis was performed using the `uvotimsum` and `uvotsource` tasks included in the `FTOOLS` software package (HEASOFT ver. 6.6.1). The latter task calculates the magnitudes through aperture photometry within a circular region and applies specific corrections due to the detector characteristics. Source counts were extracted from a circular region with a 5 arcsec radius. The background was extracted from source-free circular regions in the source surroundings. The reported magnitudes are on the UVOT photometric system described in Poole et al. (2008), and are not corrected for Galactic extinction.

3.1.3. *Swift*/*BAT*

We analyzed *Swift*/BAT Survey data in order to study the hard X-ray emission of 3C 454.3 and to investigate its evolution as a function of time.

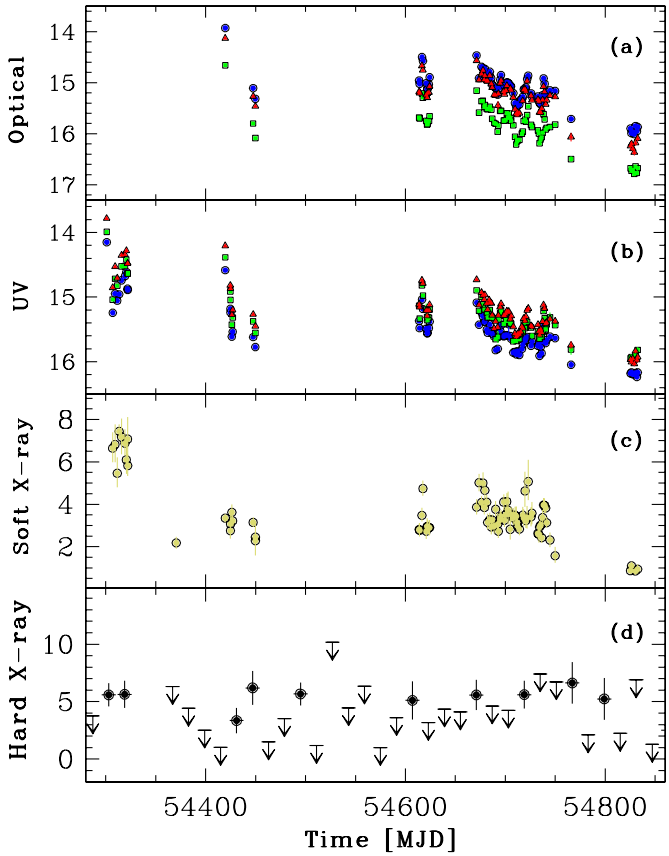

Figure 3. (a): *Swift*/UVOT light curves (observed magnitudes) in the V (red triangles), B (green squares), and U (blue circles). (b): *Swift*/UVOT light curves (observed magnitudes) in the $W1$ (red triangles), $M2$ (green squares), and $W2$ (blue circles). (c): *Swift*/XRT light curve (observed fluxes) in the 2–10 keV energy band and in units of 10^{-11} erg cm^{-2} s^{-1}. (d): *Swift*/BAT light curve in units of mCrab in the energy band 15–150 keV. Downward arrows mark 3σ upper limits.

(A color version of this figure is available in the online journal.)

We produced a light curve for the source at a 16 day binning using the procedures described in Krimm et al. (2006, 2008, and references therein; also see the Scaled Map Transient Analysis Synopsis[54]).

3.2. *Results*

Figure 3 shows the *Swift*/XRT fluxes in the 2–10 keV energy range, the *Swift*/UVOT observed magnitudes (in the V, B, U, $W1$, $M2$, and $W2$ bands), and the *Swift*/BAT fluxes in

[54] http://swift.gsfc.nasa.gov/docs/swift/results/transients/Transient_synopsis.html

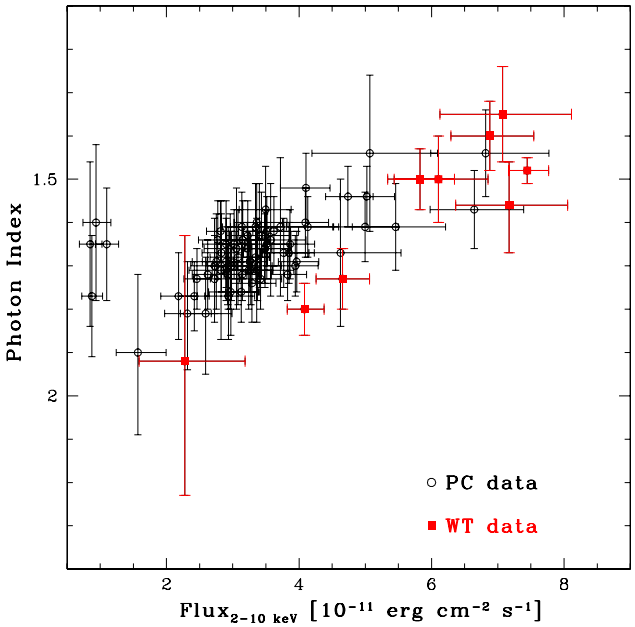

Figure 4. *Swift*/XRT photon index as a function of the 2–10 keV flux. Red squares and black circles mark the *Swift*/XRT windowed timing (WT) and photon counting (PC) data, respectively.

(A color version of this figure is available in the online journal.)

the 15–150 keV energy range as a function of time for the whole observing period. In order to diminish the statistical uncertainties, we selected observations with a number of degrees of freedom (dof) > 10. We note that a common dimming trend is present both in the UV and in the X-ray energy bands.

As shown in Figure 3, panel (d), the source has not been always detectable by *Swift*/BAT throughout the considered period, and in several time intervals only 3σ upper limits can be derived.

Figure 4 shows the *Swift*/XRT photon index as a function of the X-ray flux in the 2–10 keV energy band. Black circles and red squares represent data acquired in PC and WT mode, respectively. WT data are not affected by pile-up at the observed count rate (CR < 3 counts s^{-1}). We investigated the possible presence of a spectral trend in the X-ray data. If we consider WT data only, a "harder-when-brighter" trend seems to be present. Fitting the data with a constant model, we can exclude this model at the 99.9993% level. When analyzing the PC data only (as well as the sum of the PC and WT data), this spectral trend vanishes, and a fit with a constant model still holds. Nevertheless, if we exclude the points at fluxes $F_{2-10\,\mathrm{keV}} < 2 \times 10^{-11}$ erg cm^{-2} s^{-1} a trend still holds. These points at low fluxes could correspond to physically different state of the source than the high fluxes one.

We also note that a deep and prolonged monitoring of 3C 454.3 at mid and low X-ray states ($F_{2-10\,\mathrm{keV}} \lesssim 10^{-11}$ erg cm^{-2} s^{-1}) will be crucial to test the possible presence of a spectral trend. Our data set contains only four observations (90023002, 90023003, 90023006, and 90023008) at this flux level, which were acquired during the source low state in 2008 December.

4. *RXTE* DATA

4.1. Data Reduction and Analysis

The *RXTE* satellite observed 3C 454.3 in two epochs: from 2007 July 28 to 2007 August 04 and from 2008 May 30 to 2008 June 19. Here we report the analysis of the data obtained both with the *Proportional Counter Array* (PCA; Jahoda et al. 1996), which is sensitive in the 2–60 keV energy range, and with the High-Energy X-Ray Timing Experiment (HEXTE; Rothschild et al. 1998), which is sensitive in the 15–250 keV energy range. *RXTE* data were collected by activating a Cycle 12 ToO proposal (ID. 93150, P.I.: A.W. Chen).

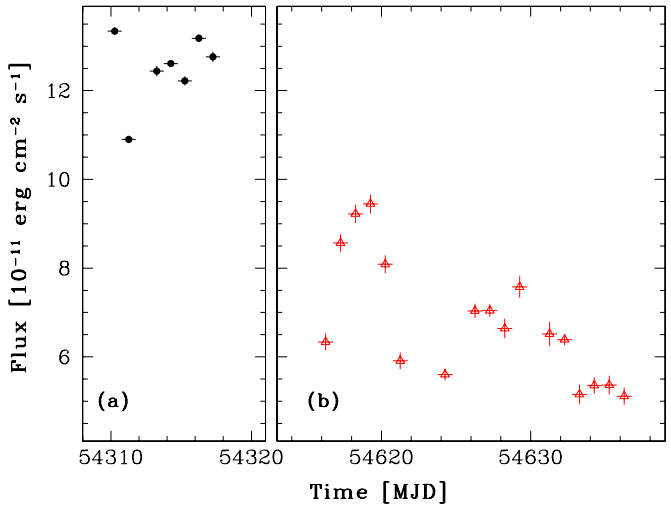

Figure 5. (a) and (b) show the *RXTE*/PCA light curve in the energy band 3–20 keV during the periods 2007 July 29–August 5 (black points) and 2008 May 30–June 19 (red triangles), respectively.

(A color version of this figure is available in the online journal.)

The PCA is composed of five identical units (Proportional Counter Units, PCUs), but during our observations only part of them were used. Since PCU2 was the only unit always on during our observations and it is the one which is best calibrated, we report the results obtained from the PCU2 data only. The data were processed using the FTOOLS ver. 6.4.1 and screened using standard filtering criteria. The net exposure times for the whole data set in the first and second epochs were 36.6 ks and 17.4 ks, respectively.

The background light curves and spectra for each observation were produced using the model appropriate to faint sources. We restricted our analysis to the 3–20 keV energy range, in order to minimize the systematic errors due to background subtraction and calibration of the *PCA* instrument.

Figure 5 shows the 3–20 keV light curve of the whole *RXTE*/PCA data set. Strong variability is observed when comparing the count rates of different observations. Moreover, the average count rate during the second epoch (panel (b)) is reduced. In order to investigate possible changes in the spectral shape with time we extracted light curves in two energy ranges (3–7 keV and 7–20 keV). Their hardness ratio did not show any significant variation.

A cumulative spectrum for the first and the second epochs was extracted and simultaneously fitted with a power-law model corrected for photoelectric absorption (`wabs*(powerlaw)` model in XSPEC), allowing only the power-law normalization to assume a different value in the two spectra. Figure 6 shows the *RXTE*/PCA spectra for both periods. A good fit (χ^2= 68.3 for 76 dof) was obtained with the following best-fit parameters (errors are at the 90% confidence level): photon index $\Gamma = 1.65 \pm 0.02$, and a flux in the 3–20 keV energy band $F_{3-20\,\mathrm{keV}} = 8.4 \times 10^{-11}$ erg cm^{-2} s^{-1} and $F_{3-20\,\mathrm{keV}} = 4.5 \times 10^{-11}$ erg cm^{-2} s^{-1} for the first and second epoch spectrum, respectively.

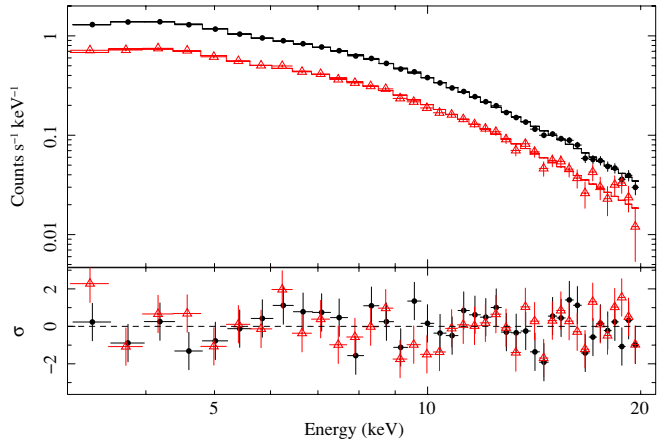

Figure 6. *RXTE*/PCA average spectra for both periods, 2007 July (black points), and 2008 May–June (red triangles), respectively.

(A color version of this figure is available in the online journal.)

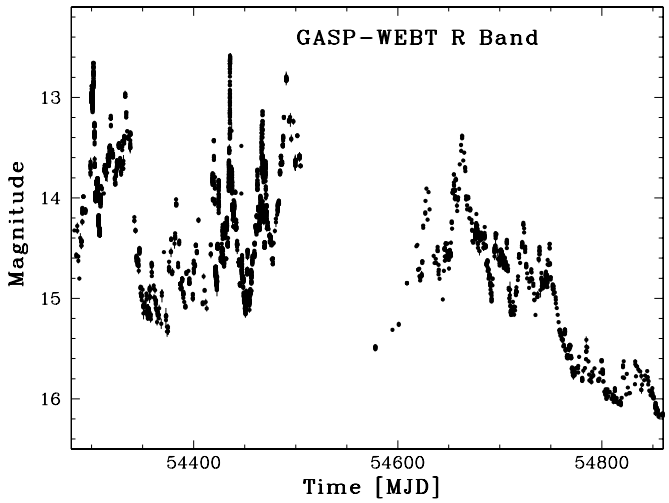

Figure 7. GASP-WEBT light curve in the *R* optical band in the 2007–2008 and 2008–2009 observing seasons.

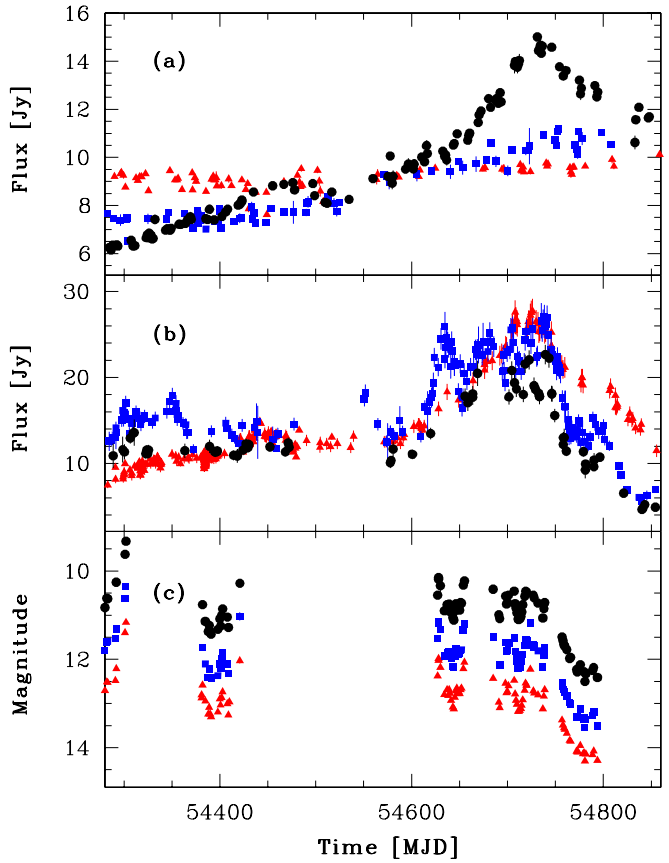

Figure 8. (a): Low-frequency radio data. Red triangles, blue squares, and black circles represent the radio flux at 5, 8, and 14.5 GHz, respectively. (b): High-frequency radio data. Red triangles, blue squares, and black circles represent the radio flux at 37, 230, and 345 GHz, respectively. (c): Near-IR data. Red triangles, blue squares, and black circles, represent the *J*, *H*, and *K* bands, respectively.

(A color version of this figure is available in the online journal.)

We note that the average *RXTE*/PCA flux during the γ-ray flare detected in 2007 July was about a factor of 2 higher than the flux detected about 10 months later. Moreover, during both the 2007 July and the 2008 May–June campaigns, the hard X-ray flux varied significantly, by about 50%, on a timescale of about one week.

We also analyzed the data of the HEXTE. Only the data from cluster B were analyzed, since the rocking system for background evaluation was disabled in the other instrument cluster. After a standard processing,[55] we extracted an average spectrum from all the available data, for a dead-time corrected exposure time of 18 ks. The source was detected up to $\sim$ 50 keV and its spectrum can be fit well (χ^2=15.1 for 19 dof) by a power-law model with a photon index of 1.6$\pm$0.1, in perfect agreement with the photon index derived from the PCA spectrum. Also, the normalization of the HEXTE spectrum is consistent with a high-energy extrapolation of the time-averaged PCA spectrum: the observed flux in the 20–40 keV energy band is $(5 \pm 3)\times10^{-11}$ erg cm^{-2} s^{-1}. This flux (approximately 6 mCrab) is also consistent with the upper limits obtained by Super-*AGILE* in the same time periods.

5. OPTICAL-TO-RADIO DATA

5.1. GASP-WEBT Data Reduction and Analysis

The WEBT[56] has been monitoring 3C 454.3 since the exceptional 2004–2005 outburst (Villata et al. 2006, 2007; Raiteri et al. 2007, 2008a, 2008b), throughout the whole period of the *AGILE* observation. We refer to Raiteri et al. (2008a, 2008b) and to Villata et al. (2009) for a detailed presentation and discussion of the radio, mm, near-IR, optical, and *Swift*/UVOT data.

Figure 7 shows the GASP-WEBT light curve in the *R* optical band, displaying several intense flares with a dynamic range of $\sim$ 2.4 mag in about 14 days, while Figure 8 shows the GASP-WEBT light curves in the near-IR (*J*, *H*, *K*), radio (5, 8, and 14.5 GHz), and mm (37, 230, and 345 GHz), respectively.[57]

6. RADIO VLBI DATA

6.1. Radio VLBI Data Reduction and Analysis

High-resolution radio VLBI data were obtained from the MOJAVE (Monitoring Of Jets in Active galactic nuclei with VLBA Experiments) project, a long-term program to monitor radio brightness and polarization variations in jets associated

[55] http://heasarc.gsfc.nasa.gov/docs/xte/recipes/hexte.html

[56] http://www.oato.inaf.it/blazars/webt, see, e.g., Villata et al. (2004).

[57] The radio-to-optical data presented in this paper are stored in the GASP-WEBT archive; for questions regarding their availability, please contact the WEBT President Massimo Villata (villata@oato.inaf.it).

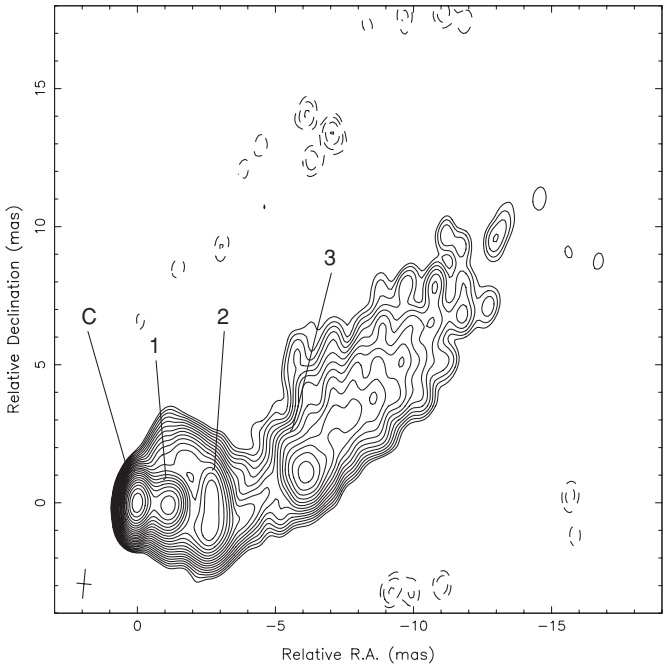

Figure 9. VLBI image of 3C 454.3 at 15 GHz on 2007 August 9 (MJD 54321). The peak flux density is 2.8 Jy beam^{-1} and contours are traced at $\pm(1, \sqrt{(2)}, 2, ...) \times 1.0$ mJy beam^{-1}. The cross in the bottom left corner shows the beam FWHM, which is 1.07 × 0.52 mas at −5.4 deg.

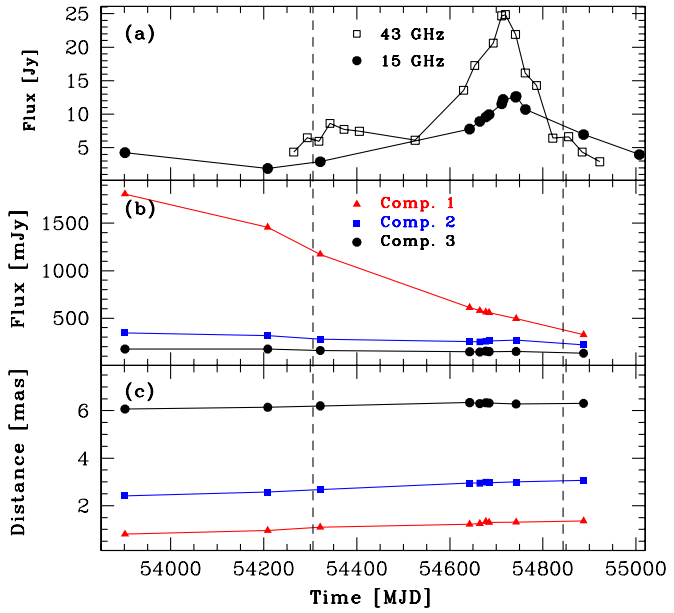

Figure 10. (a): Radio core flux density at 15 GHz (filled circles) and at 43 GHz (open squares), respectively. (b): Radio components flux density at 15 GHz. (c): Radio components motion at 15 GHz. The vertical dashed lines represent the start (2007 July 24) and the stop (2009 January 12) of all *AGILE* observations, respectively.

(A color version of this figure is available in the online journal.)

with active galaxies visible in the northern sky (Lister et al. 2009; see also[58]). The object was observed with the full VLBA at 15 GHz. We obtained the calibrated *I* images and used the AIPS package to derive the position and flux density of the core and of a few substructures in the jets using the task JMFIT (Gaussian fit; see Figure 9). Moreover, this source was additionally observed by VLBA at four epochs during the period of the maximum brightness within the BK150 VLBA experiment to measure parsec-scale spectra of γ-ray bright blazars (K. Sokolovsky et al. 2010, in preparation). We use 15 and 43 GHz results from this program to provide better radio coverage of the high activity period. These data are in agreement with MOJAVE results and give a better statistics in the high active period.

The core is always unresolved by our Gaussian fit and uncertainties on the flux density are dominated by calibration uncertainties (a few percent).

In Figure 10, we show the 3C 454.3 VLBI radio core flux (panel (a)) at 15 and 43 GHz, the radio components flux density at 15 GHz (panel (b)), and the distance of radio components from the core (panel (c)) as a function of time.

The flux shows a constant increase from 2006 June 15 (MJD 53901) till 2008 October 3 (MJD 54742), followed by a fast decrease toward the last epoch presented here, 2009 June 25 (MJD 55007). Jet components show a well defined flux density decrease (component 1) or a slower flux density decrease which becomes almost constant in the last epochs. Proper motion is evident, but slowing in time for components 1 and 2; it is almost absent for component 3.

All data are in agreement with a strong core flux density variability possibly connected to the γ-ray activity, while jet components are moving away and slowly decreasing in flux density, and are not affected by the recent core activity. In a recent paper, Kovalev et al. (2009) indeed find a connection between the radio and the γ-ray emission, correlating the *Fermi* three month data with the MOJAVE ones, and arguing that the central region of the blazars being the source of γ-ray flares. Nevertheless, a detailed study of the radio structure of 3C 454.3 is beyond the aims of this paper, therefore the jet properties will be discussed in depth elsewhere (M. L. Lister et al. 2010, in preparation; S. G. Jorstad et al. 2010, in preparation). For this reason in the following we will concentrate only on the core.

In the last two years this source has also been observed with the VLBA at 43 GHz (S. G. Jorstad et al. 2010, in preparation; see also the Boston Univ. Blazar Group VLBA Web site[59]). We used the available images to derive the flux density of the core at 43 GHz. Note that, for a better comparison with 15 GHz VLBI data, at 43 GHz we used natural weights and we have not searched for possible core subcomponents (we refer to S. G. Jorstad et al. 2010, in preparation, for a detailed study of the radio structure).

The radio core shows an inverted spectrum (self-absorbed), more evident in the high active regime, followed by a strong flux density decrease. In this region the radio spectrum is no longer inverted.

7. EIGHTEEN MONTHS OF MONITORING

In this section, we present a summary of all the observations on 3C 454.3 in the period between 2007 July 24 and 2009 January 12. The results of the campaigns performed in 2007 July, November, and December were discussed in Vercellone et al. (2008), Vercellone et al. (2009), and Donnarumma et al. (2009), respectively.

Figure 11 shows the *AGILE*/GRID light curve at ≈ 3 day resolution for $E > 100$ MeV in units of 10^{-8} photons cm^{-2} s^{-1}. The light curve shows several γ-ray flares, with a dynamical range of a factor of 3–4 on a timescale of about 10 days. Moreover, a clear dimming trend in the long-term light curve

[58] http://www.physics.purdue.edu/MOJAVE

[59] http://www.bu.edu/blazars/VLBAproject.html

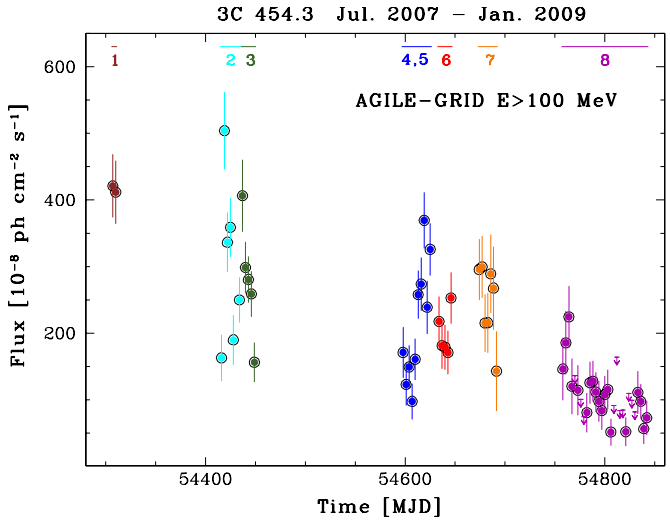

Figure 11. *AGILE*/GRID light curve at ≈ 3 day resolution for $E > 100$ MeV in units of 10^{-8} photons cm^{-2} s^{-1}. Different colors correspond to different observing campaigns, as described in Table 1.

(A color version of this figure is available in the online journal.)

is present. Table 4 shows the *AGILE*/GRID fluxes and spectral indices derived at different epochs.

7.1. Multiwavelength Light Curves

The *AGILE*/GRID wide FoV allowed for the first time a long-term monitoring of 3C 454.3 at energies above 100 MeV. Moreover, coordinated and almost simultaneous GASP-WEBT and *Swift* observations provided invaluable information on the flux and spectral behavior from radio to X-rays.

Figure 12 shows the 3C 454.3 light curves at different energies over the whole period. The different panels show, from bottom to top, the *AGILE*/GRID light curve at ≈ 1 day resolution for $E > 100$ MeV in units of 10^{-8} photons cm^{-2} s^{-1}, the *Swift*/BAT light curve in the energy range 15–150 keV at ≈ 2 week resolution, the *Swift*/XRT (filled circles) and the *RXTE*/PCA (filled squares) light curves in the energy range 3–10 keV, the *Swift*/UVOT light curve in the UV *W*2 filter, the *Swift*/UVOT light curve in the optical *B* filter, the GASP-WEBT light curve in the optical *R* filter, and the VLBI radio core at 15 GHz (filled circles) and the UMRAO 14.5 GHz (open circles) light curves, respectively.

We note that *RXTE*/PCA data are systematically higher than *Swift*/XRT ones, which is consistent with the 20% uncertainty in the relative calibrations of the two instruments in this energy band, reported by Kirsch et al. (2005).

Figure 13 shows the light curves in the *R* band, at 1.3 mm (230 GHz), and above 100 MeV. The light curve in the millimeter wavelength shows a different behavior starting from the enhanced γ-ray activity at MJD ∼ 54600, as will be discussed in Section 8.5. Moreover, starting from MJD 54750, the whole jet seems to become less energetic, with an almost monotonic flux decrease, except for a minor burst at MJD 54800.

8. DISCUSSION

In the following sections, we will discuss the correlations between the flux variations in different energy bands, the properties of the jet, and the physical parameters of the emitting source. This latter point will be addressed by means of complementary approaches, namely the SED model fitting and discussing the geometrical properties of the jet itself.

8.1. Correlation Analysis

We investigated the correlation between the γ-ray flux and the optical flux density in the *R* band by means of the discrete correlation function (DCF; Edelson & Krolik 1988; Hufnagel & Bregman 1992). This method was developed to study unevenly sampled data sets and can give an estimate of the accuracy of its results. Because of the sampling gaps in the light curves, especially at γ-rays, we calculated the DCF on four distinct periods: 2007 July (mid 2007), 2007 November–December (fall 2007), 2008 May–August (mid 2008), and 2007 October–2009 January (fall 2008). The upper limits on the γ-ray fluxes were considered as detections, with fluxes equal to one-half of the limit. In "mid 2007" AGILE was pointed at 3C 454.3 when its optical main peak was already over; furthermore, we only have five γ-ray points. The low statistics prevents us to obtain reliable results with the DCF for this period. In contrast, the period "fall 2007" offers a good opportunity to test the correlation, since the γ-ray flux, and even more the optical flux, exhibited strong variability. Moreover, the period of common monitoring lasted for more than a month. The corresponding DCF (Figure 14) shows a maximum DCF ∼ 0.38 for a null time lag. However, the shape of the peak is asymmetric, and if we calculate the centroid (Peterson et al. 1998), we find that the time lag is −0.42 days, i.e., about 10 hr. This result is in agreement with what was found by Donnarumma et al. (2009) when analyzing the 2007 December observations only, and implies that the γ-ray flux variations are delayed by few hours with respect to the optical ones. In the period "mid 2008" the main optical peak (and also the minor one) occurred when *AGILE* was not observing the source. Finally, we computed the DCF corresponding to the "fall 2008" period. We obtain a broad maximum, indicating a fair correlation ($\mathrm{DCF_{max}} \sim 0.66$), but with large errors, peaking at −2 day time lag, but with centroid around 0 day. This result is consistent with that obtained in the "fall 2007" period, which appears to be the most robust one. Hence, for this case we estimated the uncertainty on the time lag by means of the statistical method known as "flux randomization/random subset selection" (FR/RSS Peterson et al. 1998; Raiteri et al. 2003). We run 2000 FR/RSS realizations and for each of them calculated the centroid corresponding to the maximum. The resulting centroid distribution shown in Figure 14 allows us to conclude that the γ-optical correlation occurs with a time lag of $\tau = -0.4^{+0.6}_{-0.8}$, the uncertainty corresponding to a 1σ error for a normal distribution. This result is consistent with a recent analysis of the public *Fermi* data and the optical SMARTS data by Bonning et al. (2009).

8.2. Variability Analysis

The *observed* variance of a light curve for a specific detector can be written as

$$S^2 = \frac{1}{N-1}\sum_{i=1}^{N}(x_i - \bar{x})^2, \quad (5)$$

where $\bar{x}$ is the average value of the x_i measurements. Moreover, since we deal with different detectors, in order to take into account the different count rates in different energy bands, and to compare their variance, we consider the normalized variance, $S^2/\bar{x}^2$. In order to compute the *intrinsic* variance of a source light curve, the measurement errors must be taken into account, since they contribute an additional term to the variance. This approach was treated in detail by Nandra et al. (1997) and by Edelson et al.

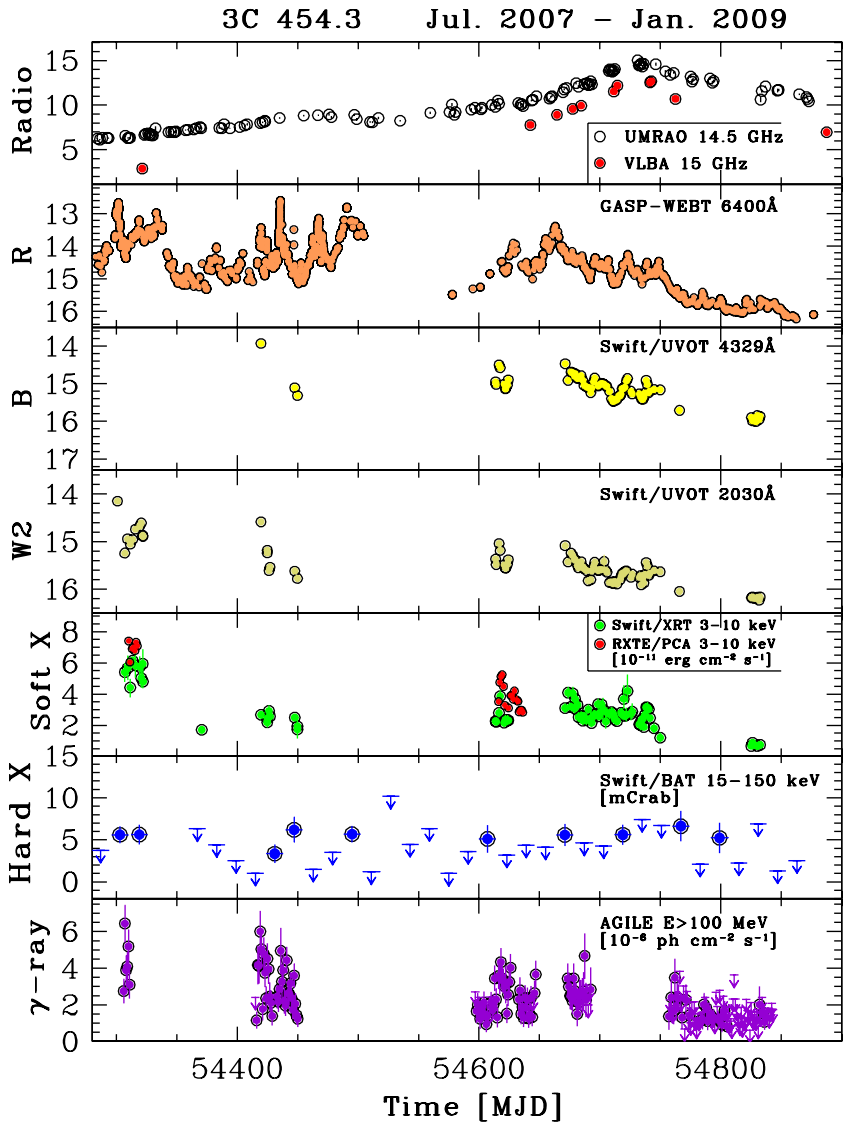

Figure 12. 3C 454.3 light curves at different energies (see Section 7.1 for details) over the whole time period.

Table 4
AGILE/GRID γ-ray Fluxes and Spectral Indices Above 100 MeV at Different Epochs

Start Time (UTC)	End Time (UTC)	$F_{E>100\,\mathrm{MeV}}$ ($\times 10^{-8}$ photons cm^{-2} s^{-1})	Γ
2007 Jul 24 14:30	2007 Jul 30 11:40	416.2 ± 36.0	1.74 ± 0.16
2007 Nov 10 12:16	2007 Dec 01 11:38	224.2 ± 15.3	1.91 ± 0.14
2007 Dec 01 11:39	2007 Dec 16 12:09	265.7 ± 17.5	1.86 ± 0.12
2008 May 10 11:00	2008 Jun 09 15:20	218.5 ± 12.2	2.05 ± 0.10
2008 Jun 15 10:46	2008 Jun 30 11:14	198.5 ± 17.1	1.98 ± 0.16
2008 Jul 25 19:57	2008 Aug 14 21:08	254.8 ± 20.6	2.11 ± 0.14
2008 Oct 17 12:51	2009 Jan 12 14:30	77.0 ± 5.5	2.21 ± 0.13

(2002), who introduced the term of "excess variance":

$$\sigma_{\mathrm{XS}}^2 = S^2 - \bar{\sigma^2}, \tag{6}$$

where $\bar{\sigma^2}$ is the mean squared error,

$$\bar{\sigma^2} = \frac{1}{N}\sum_{i=1}^{N}\sigma_i^2, \tag{7}$$

and σ_i are the measurement uncertainties of light curve points x_i.

Thus, the normalized excess variance,

$$\sigma_{\mathrm{NXS}}^2 = \frac{\sigma_{\mathrm{XS}}^2}{\bar{x^2}}, \tag{8}$$

can be used to compare variances between different observations.

In order to quantify the flux variability in different energy bands, we computed the fractional root mean square (rms)

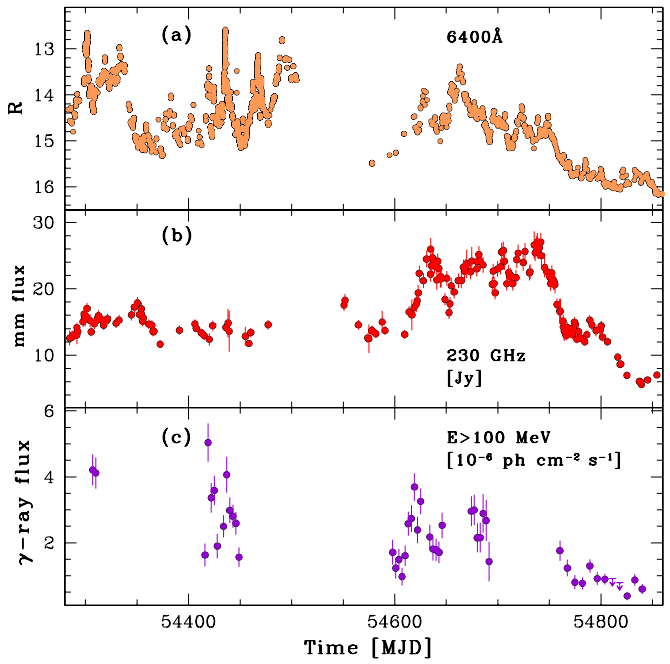

Figure 13. Comparison between the light curves in different bands. (a), (b), and (c) show the light curves in the optical, millimeter, and γ-ray energy bands, respectively.

(A color version of this figure is available in the online journal.)

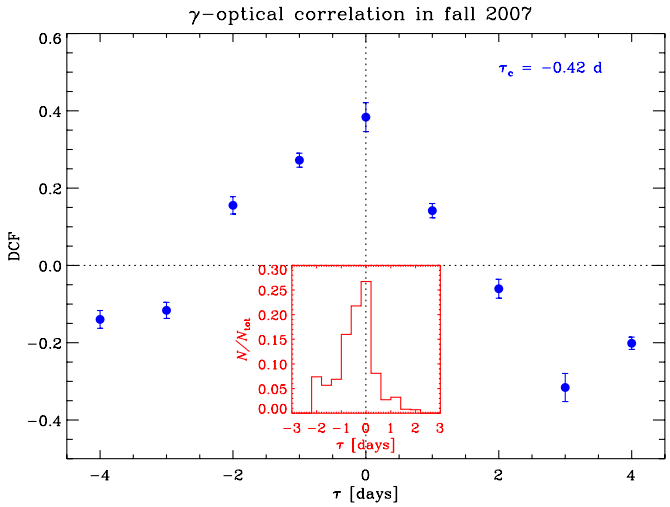

Figure 14. Discrete correlation function between the γ-ray and optical fluxes during the "fall 2007" period. The uncertainty in the time-lag can be computed according to the FR/FSS method. The inset shows the resulting centroid distribution (see Section 8.1 for details).

(A color version of this figure is available in the online journal.)

variability amplitude, $F_{\rm var}$, defined as

$$F_{\rm var} = \sqrt{\frac{S^2 - \bar{\sigma^2}}{\bar{x}^2}} \quad (9)$$

(see also Vaughan et al. 2003, and references therein).

Figure 15 shows the fractional rms variability amplitude at different frequencies. The optical R band is the one showing the highest degree of variability. This is partly due to the higher sampling of the optical data with respect to the other frequencies. Nevertheless, a possible trend (higher fractional variability amplitude at higher frequency) is also present. This

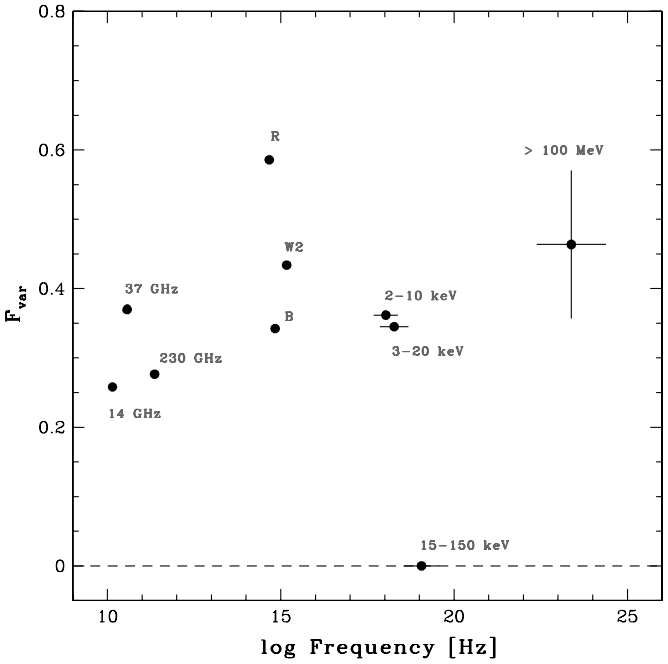

Figure 15. Fractional rms variability amplitude as a function of frequency.

possible trend of the fractional rms variability amplitude with the logarithm of the frequency was observed in other sources too (see, e.g., PKS 2155−304, Zhang et al. 2005), and it was interpreted as signature of spectral variability. A more systematic study of the variability properties of 3C 454.3 will be addressed in a forthcoming paper.

8.3. Radio VLBI versus γ-ray Data

Figure 12 clearly shows a strong enhancement of the radio core flux starting about on MJD 54500. The highest flux density is on MJD 54742 at 15 GHz and on MJD 54719 at 43 GHz. This variability is not well correlated with the variability at higher frequencies: optical and γ-ray data show more different flares in the period MJD 54400–54800 (see Figure 13, panels (a) and (c), respectively). Moreover, the radio flux density increase is smooth and longer in time, while γ-ray and optical flares are evolving faster.

At 230 GHz the flux density variability mimics the VLBI radio core properties to MJD 54600, when a large flux density increase is visible, with a peak at about MJD 54630. At this frequency the source remains in an active phase up to MJD 54700 (Figure 13(b)).

This poses an interesting question as to the nature of such an increase of the core radio flux. As reported in Ghisellini et al. (2007) it is likely that the emitting region is more compact and has a smaller bulk Lorentz factor closer to the supermassive black hole. We can assume that in the region active at 43 GHz, in the quiescent state, the jet Lorentz factor is $\Gamma \sim 10$ (Giovannini et al. 2001). To obtain the flux density increase of the core at 43 GHz (from ~ 5 Jy up to 25 Jy) the Doppler factor has to increase up to $\delta \sim 30$. Such an increase requires that the source is oriented at a small angle θ with respect to the line of sight, since a large change in the jet velocity will produce a small increase in the Doppler factor. A Doppler factor $\delta = 30$ can be obtained if $\theta = 1.^\circ5$ and $\Gamma = 20$, corresponding to a bulk velocity increase from 0.9950 to 0.9987 (note that a larger orientation angle, e.g., $\theta = 3^\circ$ with the same increase in the jet

velocity, will produce a small change in the Doppler factor δ, from 16 to 19).

The presence of one or more new jet components is not revealed in the high resolution VLBA images, even if the most recent VLBA images at 43 GHz suggest a jet expansion near to the radio core starting from MJD $\sim$ 54600. Because of different properties (multiple bursts at high frequency, a single peak in the radio band) it is not possible to correlate the radio peak with a single γ-ray or optical burst. We can speculate that a multiple source activity in the optical and γ-ray bands is integrated in the radio emitting region in a single event. This event (see Figure 10) has a clear flux density peak on MJD $\sim$ 54720 and we can assume that 43 GHz is the self-absorption frequency at that epoch. This scenario is in agreement with the one discussed by Krichbaum et al. (2008, see their Figure 3).

According to Marscher (1983), the self-absorption frequency, the source size, flux density, and the magnetic field are correlated as follows:

$$B = 3.2 \times 10^{-5} \times \theta^4 \, \nu_{\rm m}^5 \, S_{\rm m}^{-2} \, \delta \, (1+z)^{-1} \ {\rm G}, \qquad (10)$$

where B is the magnetic field in G, θ is the angular size in mas (note that $\theta = 1.8 \times$ HPBW, where HPBW is the half-power beam width), $\nu_{\rm m}$ is the frequency (in GHz) of the maximum flux density $S_{\rm m}$ (in Jy), and δ is the Doppler factor, respectively. Moreover, we assume a particular value ($\alpha = 0.5$) of spectral index in the optically thin part of the synchrotron spectrum.

Thus, we can use the radio VLBI data at 43 GHz to constrain the physical properties in the region where the source will start to be visible at this frequency. The angular resolution in the jet direction of VLBA data at 43 GHz is ~ 0.14 mas corresponding (as discussed in Marscher 1983) to $\theta \lesssim 0.25$ mas. Assuming $\delta = 30$, we obtain $B \lesssim 0.5$ G.

It is reasonable to assume that when the source is even smaller, the emission in the radio band is not visible being self-absorbed, and that the local magnetic field is $B \lesssim 0.5$ G when we start to detect the radio emission. The size of this region should be smaller than 0.25 mas (about 2 pc).

8.4. Spectral Analysis

The correlation between the flux level and the spectral slope in the γ-ray energy band was extensively studied by means of the analysis of the *EGRET* data. Nandikotkur et al. (2007) showed that the behavior of *EGRET* blazars is inhomogeneous. Figure 16 shows the *AGILE*/GRID photon index as a function of the γ-ray flux at different epochs. A "harder-when-brighter" trend seems to be present in the long timescale *AGILE* data. Further long-term observations of 3C 454.3 and of other bright γ-ray blazars at different flux levels with *AGILE* and *Fermi* will be crucial to assess this topic.

Different emission mechanisms can be invoked to explain the γ-ray emission. In the leptonic scenario, the low-frequency peak in the blazar SED is interpreted as synchrotron radiation from high-energy electrons in the relativistic jet, while the high-energy peak can be produced by IC on different kinds of seed photons. In the synchrotron self-Compton (SSC) model (Ghisellini et al. 1985; Bloom & Marscher 1996) the seed photons come from the jet itself. Alternatively, the seed photons can be those of the accretion disk (external Compton scattering of direct disk radiation, ECD; Dermer et al. 1992) or those of the BLR clouds (external Compton scattering from clouds, ECC; Sikora et al. 1994). The target seed photons can also be those produced by the dust torus surrounding the nucleus

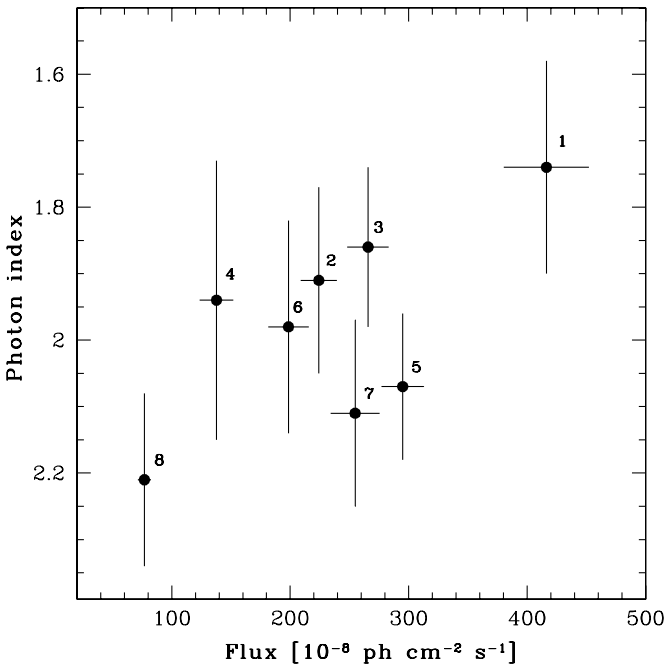

Figure 16. *AGILE*/GRID photon index as a function of the γ-ray flux above 100 MeV. Numbers beside each points represent the epochs listed in Table 1.

(external Compton scattering from IR-emitting dust, ERC(IR); Sikora et al. 2002).

We fit the SEDs for the different observing periods by means of a one-zone leptonic model, considering the contributions from SSC and from external seed photons originating both from the accretion disk and from the BLR (detailed description of this model is given in Vittorini et al. 2009). Indeed, emission from both of them were detected during faint states of the source (Raiteri et al. 2007).

The emission along the jet is assumed to be produced in a spherical blob with comoving radius R by accelerated electrons characterized by a comoving broken power-law energy density distribution of the form

$$n_e(\gamma) = \frac{K \gamma_{\rm b}^{-1}}{(\gamma/\gamma_{\rm b})^{\alpha_{\rm l}} + (\gamma/\gamma_{\rm b})^{\alpha_{\rm h}}}, \qquad (11)$$

where γ is the electron Lorentz factor assumed to vary between $10 < \gamma < 10^4$, $\alpha_{\rm l}$ and $\alpha_{\rm h}$ are the pre- and post-break electron distribution spectral indices, respectively, and $\gamma_{\rm b}$ is the break energy Lorentz factor. We assume that the blob contains a homogeneous and random magnetic field B and that it moves with a bulk Lorentz Factor Γ at an angle Θ_0 with respect to the line of sight. The relativistic Doppler factor is then $\delta = [\Gamma (1 - \beta \cos \Theta_0)]^{-1}$, where β is the usual blob bulk speed in units of the speed of light.

Our modeling of the 3C 454.3 high-energy emission is based on an IC model with two main sources of external target photons: (1) an accretion disk characterized by a blackbody spectrum peaking in the UV with a bolometric luminosity $L_{\rm d}$ for an IC-scattering blob at a distance $r_{\rm d} = 4.6 \times 10^{16}$ cm from the central part of the disk; and (2) a BLR with a spectrum peaking in the V band, placed at a distance from the blob of $r_{\rm BLR} = 4 \times 10^{18}$ cm, and assumed to reprocess 10% of the irradiating continuum (Tavecchio & Ghisellini 2008; Raiteri et al. 2007, 2008b).

These two regions contribute to the ECD and the ECC, respectively, and it is interesting to test the relative importance of the two components that can be emitted by the relativistic jet

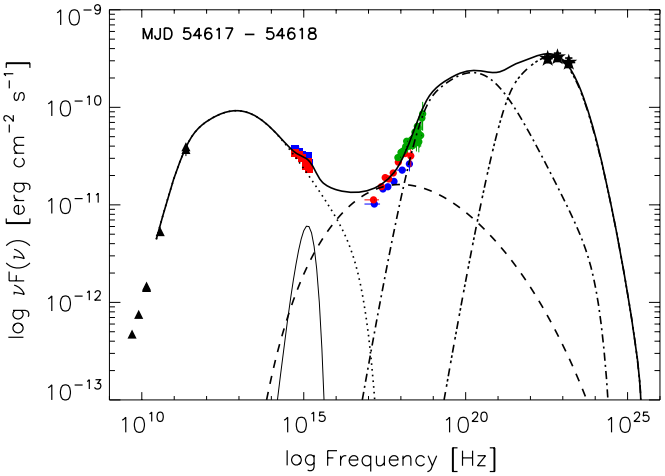

Figure 17. 3C 454.3 SED centered on MJD 54617–54618. Black triangles, red (blue) squares, red (blue) circles, green circles, and black stars represent radio, MJD 54617 (54618) *Swift*/UVOT, MJD 54617 (54618) *Swift*/XRT, *RXTE*/PCA, and *AGILE*/GRID data, respectively. UV and X-ray data are de-reddened and corrected for Galactic extinction. The thin solid, dotted, dashed, dot-dashed, and the triple-dot-dashed, represent the accretion disk blackbody, the synchrotron, the SSC, the external Compton on the disk, and the external Compton on the BLR radiation, respectively. The thick solid line represents the sum of all the individual components.

(A color version of this figure is available in the online journal.)

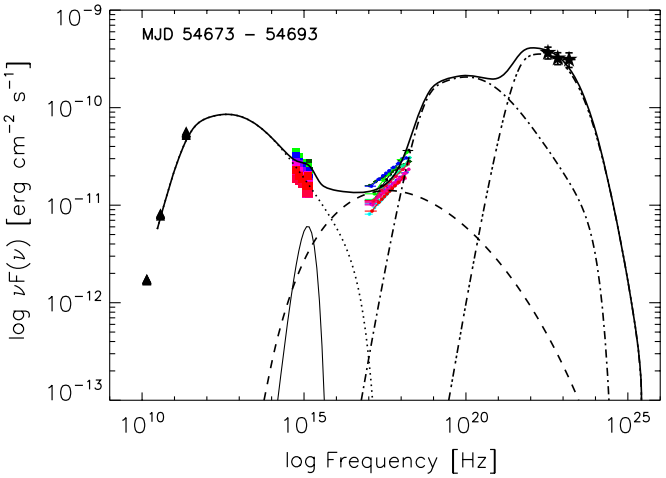

Figure 18. 3C 454.3 SED during the period MJD 54673–54693. Black triangles, multicolor squares, circles, and black stars represent radio, *Swift*/UVOT, *Swift*/XRT, and *AGILE*/GRID data, respectively. UV and X-ray data are de-reddened and corrected for Galactic extinction. The thin solid, dotted, dashed, dot-dashed, and the triple-dot-dashed, represent the accretion disk blackbody, the synchrotron, the SSC, the external Compton on the disk, and the external Compton on the BLR radiation, respectively. The thick solid line represents the sum of all the individual components.

(A color version of this figure is available in the online journal.)

Table 5
Input Parameters for the Model of SED1, SED2, and SED3

Parameter	SED1	SED2	SED3	Units
α_l	2.3	2.5	2.0	
α_h	4.0	4.0	4.2	
γ_{min}	30	30	18	
γ_b	300	280	180	
K	80	80	100	cm^{-3}
R	21.5	21.5	21.5	10^{15} cm
B	2	2	2	G
δ	34	34	34	
L_d	5	5	5	10^{46} erg s^{-1}
r_d	0.015	0.015	0.015	pc
Θ_0	1.15	1.15	1.15	degrees
Γ	20	20	20	
P_{jet}	3.2	3.7	2.5	10^{46} erg s^{-1}

Note. See Section 8.5 for details.

of 3C 454.3 under different conditions. We summarize here the main results of our best model for the different time periods.

Table 5 shows the best-fit parameters of our modeling of SEDs corresponding to the following periods (see Figure 1): (SED1), MJD 54617–54618, when 3C 454.3 entered a phase of high γ-ray activity; (SED2) MJD 54673–54693, when the γ-ray flux was almost constant; (SED3) MJD 54800–54845, when the source flux was at the minimum level (about 70×10^{-8} photons cm^{-2} s^{-1}). In Figures 17, 18, and 19, the thin solid, dotted, dashed, dot-dashed, and the triple-dot-dashed, represent the accretion disk blackbody, the synchrotron, the SSC, the external Compton on the disk, and the external Compton on the BLR radiation, respectively, while the thick solid line represents the sum of all the individual components. The inset of Figure 19 shows the portion of the SED dominated by the contribution of the disk blackbody radiation, which clearly emerges since the source is a relative low state.

We find that the three SEDs can be reproduced well by very similar parameters, the main difference being the shape of the

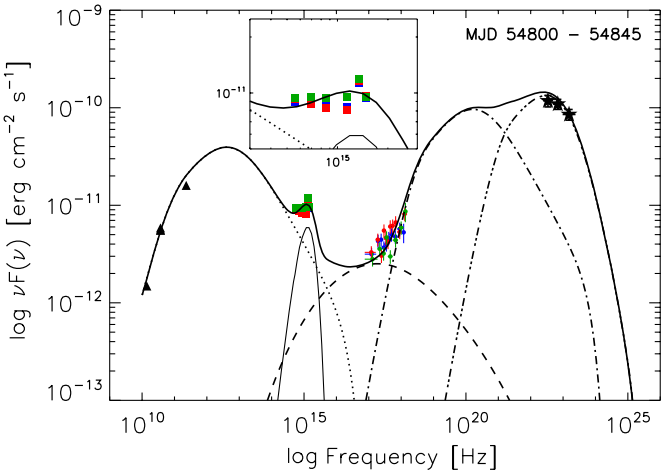

Figure 19. 3C 454.3 SED during the period MJD 54800–54845. Black triangles, multicolor squares, circles, and black stars represent radio, *Swift*/UVOT, *Swift*/XRT, and *AGILE*/GRID data, respectively. UV and X-ray data are de-reddened and corrected for Galactic extinction. The thin solid, dotted, dashed, dot-dashed, and the triple-dot-dashed, represent the accretion disk blackbody, the synchrotron, the SSC, the external Compton on the disk, and the external Compton on the BLR radiation, respectively. The thick solid line represents the sum of all the individual components. The inset shows the portion of the SED dominated by the contribution of the disk blackbody radiation.

(A color version of this figure is available in the online journal.)

electron distribution and the break energy Lorentz factor. We note that the observed minimum variability timescale, of the order of half a day, is consistent with the minimum variability timescale ($\sim$ 10 hr) allowed by the model fit. Finally, we computed for the three different SEDs the total power carried in the jet, P_{jet}, defined as

$$P_{jet} = L_B + L_p + L_e + L_{rad} \ \ \mathrm{erg\,s^{-1}}, \qquad (12)$$

where L_B, L_p, L_e, and L_{rad} are the power carried by the magnetic field, the cold protons, the relativistic electrons, and the produced radiation, respectively. We obtain a value of P_{jet} of

3.2×10^{46} erg s^{-1}, 3.7×10^{46} erg s^{-1}, and 2.5×10^{46} erg s^{-1} for SED1, SED2, and SED3, respectively. The total power of the jet is lower at the end of the *AGILE* observing period, following the general trend of the multiwavelength light curves.

8.5. Jet Geometry

The light curves in Figure 13 show a different behavior starting from the end of 2007 among the different energy bands.

As shown in Villata et al. (2009), a possible interpretation arises in the framework of a change in orientation of a curved jet, yielding different alignment configurations within the jet itself.

During 2007, the more pronounced fluxes and variability of the optical and γ-ray bands seem to favor the inner portion of the jet as the more beamed one. On the other hand, the dimming trend in the optical and in the γ-ray bands, the higher mm flux emission and its enhanced variability during 2008, seem to indicate that the more extended region of the jet became more aligned with respect to the observer line of sight.

9. CONCLUSIONS

The *AGILE* high-energy long-term monitoring of the blazar 3C 454.3 allowed us to organize a few multiwavelength campaigns, as well as monitoring programs at lower frequencies, over a time period of about 18 months. Thus, we were able to investigate the SEDs over several decades in energy, to study the interplay between the γ-ray and the optical fluxes, and the physical properties of the jet producing the non-thermal radiation.

The *global* view we obtained after one and a half years of observations can be summarized as follows.

1. The γ-ray emission for energy $E > 100$ MeV is clearly highly variable, on timescales of the order of 1 day or even shorter, with prominent flares reaching, on a day timescale, the order of magnitude of the Vela pulsar emission, the brightest, persistent γ-ray source above 100 MeV.
2. Starting from 2008 October, 3C 454.3 entered a prolonged mid- to low-level γ-ray phase, lasting several months.
3. Emission in the optical range appears to be weakly correlated with that at γ-ray energies above 100 MeV, with a lag (if present) of the γ-ray flux with respect to the optical one less than 1 day.
4. While at almost all frequencies the flux shows a diminishing trend with time, the 15 GHz radio core flux increases, although no new jet component seems to be detected.
5. The average γ-ray spectrum during the different observing campaigns seems to show a harder-when-brighter trend.
6. Our results support the idea that the dominant emission mechanism in γ-ray energy band is the IC scattering of external photons from the BLR clouds scattering off the relativistic electrons in the jet.
7. The different behavior of the light curves at different wavelengths could be interpreted by a changing of the jet geometry between 2007 and 2008.

The simultaneous presence of two γ-ray satellites, *AGILE* and *Fermi*, the extremely prompt response of wide-band satellites such as *Swift*, and the long-term monitoring provided from the radio to the optical by the GASP-WEBT Consortium will assure the chance to investigate and study the physical properties of several blazars both at high and low emission states.

The *AGILE* Mission is funded by the Italian Space Agency (ASI) with scientific and programmatic participation by the Italian Institute of Astrophysics (INAF) and the Italian Institute of Nuclear Physics (INFN). This investigation was carried out with partial support under ASI Contract No. I/089/06/1. We acknowledge financial support by the Italian Space Agency through contract ASI-INAF I/088/06/0 for the Study of High-Energy Astrophysics. This work is partly based on data taken and assembled by the WEBT collaboration and stored in the WEBT archive at the Osservatorio Astronomico di Torino - INAF.[60] We thank the *Swift* and *RXTE* Teams for making these observations possible, particularly the duty scientists and science planners. This research has made use of data from the MOJAVE database that is maintained by the MOJAVE team. The 70 cm meniscus observations was partially supported by Georgian National Science Foundation grant GNSF/ST-08/4-404. E.K. acknowledges support from the NCS grant No. 96-2811-M-008-033. K. Sokolovsky was supported by the International Max Planck Research School (IMPRS) for Astronomy and Astrophysics at the Universities of Bonn and Cologne. We thank L. Fuhrmann for collaborating in the setup of the *AGILE*/*Fermi Swift* monitoring campaign in the period 2008 August–October. We also thank the referee for his/her constructive comments.

Facilities: AGILE, *Swift*, *RXTE*, WEBT, VLBA, UMRAO

REFERENCES

Abdo, A. A., et al. 2009, ApJ, 699, 817
Anderhub, H., et al. 2009, A&A, 498, 83
Bloom, S. D., & Marscher, A. P. 1996, ApJ, 461, 657
Bonning, E. W., et al. 2009, ApJ, 697, L81
Burrows, D. N., et al. 2005, Space Sci. Rev., 120, 165
Celotti, A., & Ghisellini, G. 2008, MNRAS, 385, 283
Dermer, C. D., Schlickeiser, R., & Mastichiadis, A. 1992, A&A, 256, L27
Donnarumma, I., et al. 2008, ATel, 1545, 1
Donnarumma, I., et al. 2009, ApJ, 707, 1115
Edelson, R. A., & Krolik, J. H. 1988, ApJ, 333, 646
Edelson, R., Turner, T. J., Pounds, K., Vaughan, S., Markowitz, A., Marshall, H., Dobbie, P., & Warwick, R. 2002, ApJ, 568, 610
Feroci, M., et al. 2007, Nucl. Instrum. Methods Phys. Res. A, 581, 728
Fuhrmann, L., et al. 2006, A&A, 445, L1
Gasparrini, D., et al. 2008, ATel, 1592, 1
Gehrels, N., et al. 2004, ApJ, 611, 1005
Ghisellini, G., Foschini, L., Tavecchio, F., & Pian, E. 2007, MNRAS, 382, L82
Ghisellini, G., Maraschi, L., & Treves, A. 1985, A&A, 146, 204
Giommi, P., et al. 2006, A&A, 456, 911
Giovannini, G., Cotton, W. D., Feretti, L., Lara, L., & Venturi, T. 2001, ApJ, 552, 508
Giuliani, A., Chen, A., Mereghetti, S., Pellizzoni, A., Tavani, M., & Vercellone, S. 2004, Mem. Soc. Astron. Ital. Suppl., 5, 135
Hartman, R. C., et al. 1999, ApJS, 123, 79
Hartman, R. C., et al. 2001a, ApJ, 553, 683
Hartman, R. C., et al. 2001b, ApJ, 558, 583
Hufnagel, B. R., & Bregman, J. N. 1992, ApJ, 386, 473
Jahoda, K., Swank, J. H., Giles, A. B., Stark, M. J., Strohmayer, T., Zhang, W., & Morgan, E. H. 1996, Proc. SPIE, 2808, 59
Kirsch, M. G., et al. 2005, Proc. SPIE, 5898, 22
Kovalev, Y. Y., et al. 2009, ApJ, 696, L17
Krichbaum, T. P., et al. 2008, in ASP Conf. Ser. 386, Extragalactic Jets: Theory and Observation from Radio to Gamma Ray, ed. T. A. Rector & D. S. De Young (San Francisco, CA: ASP), 186
Krimm, H. A., Barthelmy, S. D., Cummings, J. R., Markwardt, C. B., Skinner, G., & Tueller, J. (Swift/BAT Team) 2008, BAAS, 40, 07.01
Krimm, H., et al. 2006, ATel, 904, 1
Labanti, C., et al. 2009, Nucl. Instrum. Methods Phys. Res. A, 598, 470
Lister, M. L., et al. 2009, AJ, 137, 3718
Marscher, A. P. 1983, ApJ, 264, 296
Mattox, J. R., et al. 1993, ApJ, 410, 609

[60] http://www.oato.inaf.it/blazars/webt/archive.html

Mücke, A., & Protheroe, R. J. 2001, Astropart. Phys., 15, 121
Mücke, A., Protheroe, R. J., Engel, R., Rachen, J. P., & Stanev, T. 2003, Astropart. Phys., 18, 593
Nandikotkur, G., Jahoda, K. M., Hartman, R. C., Mukherjee, R., Sreekumar, P., Böttcher, M., Sambruna, R. M., & Swank, J. H. 2007, ApJ, 657, 706
Nandra, K., George, I. M., Mushotzky, R. F., Turner, T. J., & Yaqoob, T. 1997, ApJ, 476, 70
Perotti, F., Fiorini, M., Incorvaia, S., Mattaini, E., & Sant'Ambrogio, E. 2006, Nucl. Instrum. Methods. Phys. Res. A, 556, 228
Peterson, B. M., Wanders, I., Horne, K., Collier, S., Alexander, T., Kaspi, S., & Maoz, D. 1998, PASP, 110, 660
Pian, E., et al. 2006, A&A, 449, L21
Pittori, C., et al. 2008, ATel, 1634, 1
Poole, T. S., et al. 2008, MNRAS, 383, 627
Prest, M., Barbiellini, G., Bordignon, G., Fedel, G., Liello, F., Longo, F., Pontoni, C., & Vallazza, E. 2003, Nucl. Instrum. Methods Phys. Res. A, 501, 280
Raiteri, C. M., et al. 2003, A&A, 402, 151
Raiteri, C. M., et al. 2007, A&A, 473, 819
Raiteri, C. M., et al. 2008a, A&A, 485, L17
Raiteri, C. M., et al. 2008b, A&A, 491, 755
Rothschild, R. E., et al. 1998, ApJ, 496, 538
Sikora, M., Begelman, M. C., & Rees, M. J. 1994, ApJ, 421, 153
Sikora, M., Błażejowski, M., Moderski, R., & Madejski, G. M. 2002, ApJ, 577, 78
Tavani, M., et al. 2008, Nucl. Instrum. Methods Phys. Res. A, 588, 52
Tavani, M., et al. 2009, A&A, 502, 995
Tavecchio, F., & Ghisellini, G. 2008, MNRAS, 386, 945
Tosti, G., Chiang, J., Lott, B., Do Couto E Silva, E., Grove, J. E., & Thayer, J. G. 2008, ATel, 1628, 1
Vaughan, S., Edelson, R., Warwick, R. S., & Uttley, P. 2003, MNRAS, 345, 1271
Vercellone, S., et al. 2007, ATel, 1160, 1
Vercellone, S., et al. 2008, ApJ, 676, L13
Vercellone, S., et al. 2009, ApJ, 690, 1018
Villata, M., et al. 2004, A&A, 424, 497
Villata, M., et al. 2006, A&A, 453, 817
Villata, M., et al. 2007, A&A, 464, L5
Villata, M., et al. 2009, A&A, 504, L9
Vittorini, V., et al. 2008, ATel, 1581, 1
Vittorini, V., et al. 2009, ApJ, 706, 1433
Zhang, Y. H., Treves, A., Celotti, A., Qin, Y. P., & Bai, J. M. 2005, ApJ, 629, 686